Numerical simulation of a riveted helicopter panel during a ditching maneuver

Guagliardo Davide[1], Cestino Enrico[1], Gaglione Pietro[2], Trofa Stanislao[2], Di Nuzzo Salvatore[2] and Liquori Ferdinando[2]

[1] Department of Mechanical and Aerospace Engineering, Polytechnic of Turin, Turin, Italy
[2] Capgemini Engineering

1 Abstract

The following study aims to present an impact analysis in water of a simplified geometry of a riveted helicopter panel. The analyses were conducted using Ls-Dyna solver, applying the FEM methodology to simulate the impacting body and the water, which was modelled using the SPH (Smoothed-Particle Hydrodynamics) method. The study focuses specifically on a geometry representing an aluminium box of dimensions compatible with those found in the underfloor areas of helicopters. In the first part of the paper, different types of rivet models will be investigated considering a single riveted lap joint under tension, highlighting the best choice especially when elastic-plastic behaviour should be considered.
The focus will be, in the second part, on the forces that develop on the bottom plate and the rivets connecting the plate to the two reinforcement elements, namely the stringers and frames, during a ditching maneuver. A comparison will be conducted between the measured pressures and those projected by analytical theories. Additionally, the influence of air-cushioning will be investigated, discussing the benefits and the conditions under which it can be neglected.

2 Introduction

The study of water impacts, known as 'ditching,' is a recurring issue whenever discussing safety in the aeronautical and maritime fields. The first to analytically study the behaviour were von Karman [1] and Wagner [2], with the former basing his work on the conservation of momentum, and the latter focusing on the hydrodynamic effects of water. Subsequently, other theories were developed [3, 4, 5] to address cases where the previous models prove inadequate, specifically for bodies with small or zero dihedral angles. In fact, the problem of water impacts is extremely complex, as it requires consideration of hydrodynamic phenomena that may arise, including air cushioning, ventilation, suction, and cavitation. These phenomena manifest with varying intensity depending on the body's geometry and deformability [4, 5].
This work presents a practical case of aeronautical interest concerning the water landing of a simplified helicopter subfloor model (Figure 1), focusing on the riveted joints located on the connecting flanges. Moreover, since the subfloor of any helicopter has a zero inclination, at least locally at the point of first impact, analyses were conducted with low dihedral angles, which represent the most critical cases.

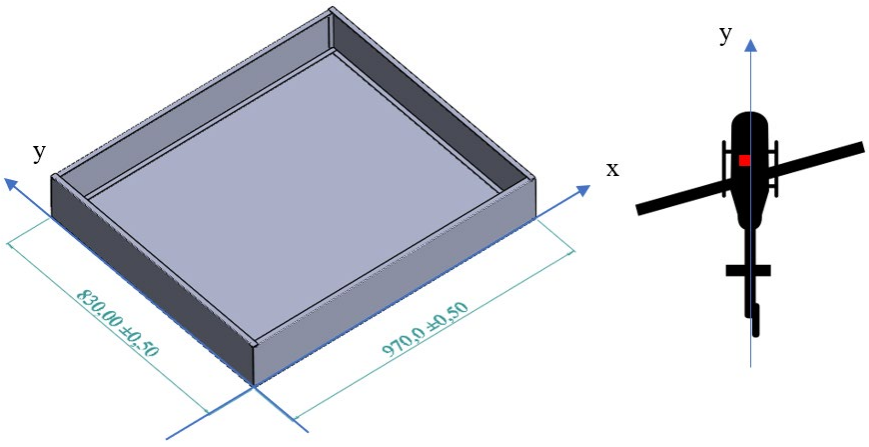

Fig.1: Geometry considered in water impact analyses

It is well known that the structural loads encountered during water impacts are entirely different from those experienced in hard surface impacts [6]. This is due to the fact that the primary components designed to absorb energy through their progressive collapse (landing gear, crossbeams, crushable bars and seats) are not efficiently utilized. In a ground impact, the loads are evenly distributed across the energy-absorbing structures, and the skin panels do not deform, contributing minimally (Figure 2). In contrast, during a water impact, the forces are uniformly distributed across the subfloor but are insufficient to trigger the collapse of the frame. This leads to high vertical accelerations, excessive deflection of the panels (Figure 3), and subsequent rivet failure.

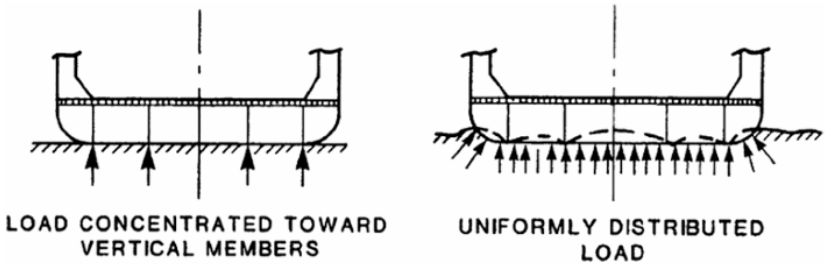

Fig.2: Difference in load transmission during a hard impact (left) and a water impact (right)

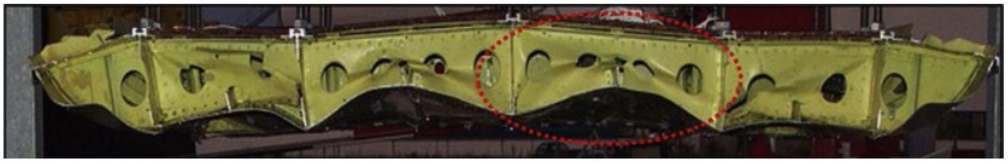

Fig.3: Water impact of a helicopter subfloor [7]

3 Rivet modelling

The objective of this paragraph is to determine the formulation of the elements that will be used in the model impacting the water. The rivets considered are the MS20470AD5-5 (Figure 4), commonly used in the aerospace industry for helicopter construction.

Fig.4: MS20470AD5-5 rivets

Through explicit computational software, rivets can be simulated in various ways that differ in terms of their modelling and formulation. The first method, which is the most computationally expensive, involves creating a 3D geometry. While highly effective, as demonstrated by Langard et al. [8], it is also computationally demanding. This option was not explored, as it would have added further computational cost to an already complex model due to the simulation of water and air using the SPH method.
Preliminary analyses were performed using this type of connection to study its characteristics. Below is the model (Figure 5), consisting of two overlapping plates and two rivets, symmetrically positioned at the nodes highlighted in blue. Additionally, the image shows the boundary nodes highlighted in red, where all translations are constrained. The two plates are square, with a side length of 100 mm and a thickness of 2 mm, and are discretized using shell elements with a size of 5 mm. The material is defined using the **`*MAT_ELASTIC`** keyword and has the properties of standard steel, as shown in Table 1.
Both analyses with purely axial force and purely shear force were conducted. All cases with purely axial force produced satisfactory results, while those with purely shear force revealed limitations in some of the formulations used. Therefore, the following discussion includes, for brevity, only simulations where a shear force is applied in the positive y-direction, distributed across the edge nodes of the lower plate.

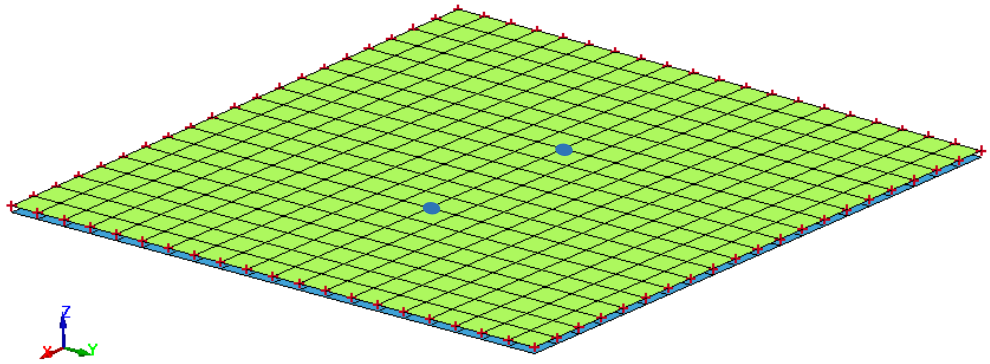

Fig.5: Plates with rivets and constrained nodes

Density	7.850 x 10^{-6} Kg/mm^3
Young's modulus	210 GPa
Poisson's ratio	0.33

Table 1: Mechanical properties

The following sections will present the three methods investigated in order to select the most suitable one.

3.1 Nodal connection

Using the **`*CONSTRAINED_RIVET`** keyword, it is possible to create a kinematic link between two non-coincident nodes [10]. This does not create an actual rivet with its own mass, nor is a failure criterion specified. A failure time (TF) can be defined, after which the constraint is deactivated.
The total load applied to the 21 edge nodes is 1 N, increasing from 0 to 1 N over 100 ms, after which it remains constant until the end of the simulation. The results show an oscillatory pattern of forces on the rivets, which lacks physical correlation. Specifically, as seen in Figure 6, this type of connection fails to handle and transmit shear forces, which for the two rivets are superimposed and equal to zero. Instead, it transmits an oscillatory axial load, with an average value significantly different from the applied load. While the forces on the two rivets exhibit symmetry, as expected, the results are not satisfactory.

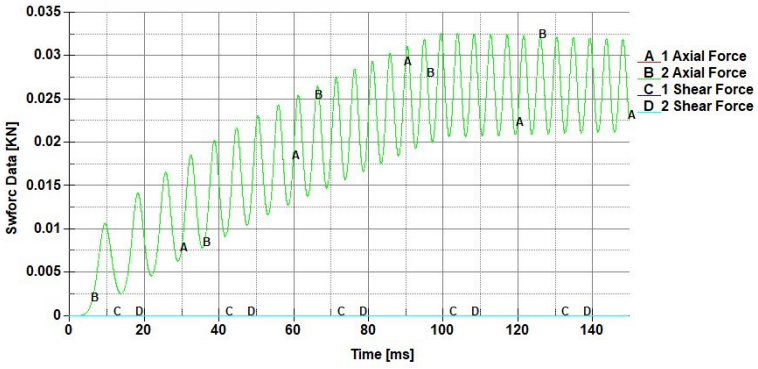

Fig.6: Resulting loads on the two rivets under pure transverse force

Additionally, this type of connection is more effective when the connected nodes do not have rotary inertias, such as when the nodes belong to solid elements

3.2 Rigid connectors

To investigate the nature of the oscillations, other options provided by the software were explored. Specifically, techniques allowing the creation of a connection through a rigid body placed between two non-coincident nodes were investigated.
The two formulations considered are those defined by the **`*CONSTRAINED_RIGID_BODY`** and **`*CONSTRAINED_SPOTWELD`** keywords. In both cases, translations and rotations are coupled, without

allowing for any elongation in the connection. In the first case, it is not possible to specify a failure criterion; in the second case, however, failure parameters can be defined for both axial and transverse directions, supporting both brittle and ductile failure modes. These failure types differ in their mechanisms: the first is summative, based on the resultant forces in the connection, while the second occurs when the average plastic strain of the shell elements surrounding the connected node exceeds the threshold value.
Due to its characteristics, the ***CONSTRAINED_SPOTWELD** formulation is designed for spot welds but could be applied to rivets in the following scenarios:

- The number of rivets is high, leading to potential failure in the sheets;
- The rivet material is not very ductile, assuming of no plastic deformation applicable.

In general, both formulations are node-dependent, which requires refining and regularizing the mesh around the joint. This issue can be addressed by creating a third element, as discussed in the following section.

3.3 Elastoplastic beam

The final formulation presented for modelling rivet joints in simulations involves the use of a 1D element called a "beam," defined using the ***ELEMENT_BEAM** keyword. This approach offers an optimal balance between accuracy and computational time. On one hand, it allows for the assignment of properties that make the element as realistic as possible; on the other hand, it reduces the timestep, thereby increasing the computational time due to the small size of the element.
For this type of element, it is necessary to define a ***SECTION_BEAM**, shown in Table 2, to assign geometric characteristics, and to specify a material using the ***MAT_SPOTWELD** keyword to assign mechanical properties.

ELFORM (Element formulation)	9
CST (Cross Section Type)	1 (tubular)
Outer diameter	4 mm
Inner diameter	0 mm

*Table 2: ***SECTION_BEAM** card*

The rivet is made of an aluminium alloy 2117 – T4, while the plate is made of an aluminium alloy 2024 – T3, assigned through the ***MAT_PIECEWISE_LINEAR_PLASTICITY** keyword. The material parameters and failure criteria were obtained from the literature [10, 11]. As for the failure forces of the rivets, they were set in these analyses to a maximum axial component of 3 kN and a maximum shear component of 2 kN. These values were chosen arbitrarily to approximate real-world conditions while allowing for easier verification of the results. However, for the complete model discussed in the following section, the actual failure values of the rivets, as reported in [10], were used. The failure criterion is based on the achievement of the unit value by the sum of the forces on the rivets in relation to the chosen maximum value. This can be summarized in the following equation:

$$\left(\frac{N_{rr}}{N_{rrF}}\right)^2 + \left(\frac{N_{rs}}{N_{rsF}}\right)^2 + \left(\frac{N_{rt}}{N_{rtF}}\right)^2 = 1$$

In its complete form, the results also account for the moments, which have been disregarded in this study. Specifically, the values in the numerator represent the forces measured during the simulation in the axial direction (the first) and in the two shear directions (the others). The denominator, on the other hand, consists of the maximum attainable values defined in the keyword. By defining N_{RS} and N_{RT} as identical, it is assumed that the material exhibits isotropic behaviour in the two shear directions.

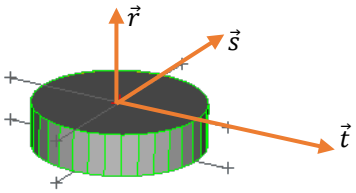

Once the element is created, it must be connected to the plates it is meant to join. This can be achieved by either connecting the ends of the rivet to the mesh nodes using rigid elements or by defining a contact between the element and the plates. The connection via rigid elements is highly dependent on the mesh, and for this reason, it was discarded, despite yielding similar results in a simple case to those obtained when contact was defined. On the other hand, the contact-based approach is particularly interesting because it is not dependent on the mesh nodes, although it provides better results when the rivet is located at the centre of a model element.
The chosen contact keyword was ***CONTACT_TIED_SHELL_EDGE_TO_SURFACE**, which couples both rotations and translations. In this setup, the plate is defined as the master, and the beam as the slave.

3.3.1 Analyses conducted

After defining the formulation and geometry of the rivets, a series of analyses was conducted to refine the parameters for the upcoming water impact simulations. These analyses involved a different configuration in which the formulation of the plates and the magnitude of the shear force were varied, along with secondary parameters such as the friction between the plates.
The new analyses consisted of two plates modeled using shell elements with formulation 16 (fully integrated) and hourglass control type 8. This was necessary to eliminate the phenomenon of "shear locking." Both plates had dimensions of 300 x 456 mm and a thickness of 1 mm. The plates were overlapped by a width of 12 mm, as shown in Figure 7, with the rivets located at the center. There were 10 rivets, each with a diameter of 4 mm, positioned 26 mm from the outer edge and spaced 28 mm apart, except for the lowest rivet, which was 24 mm from the previous one. This detail is important, as it will become evident in the analysis of the forces on the rivets.

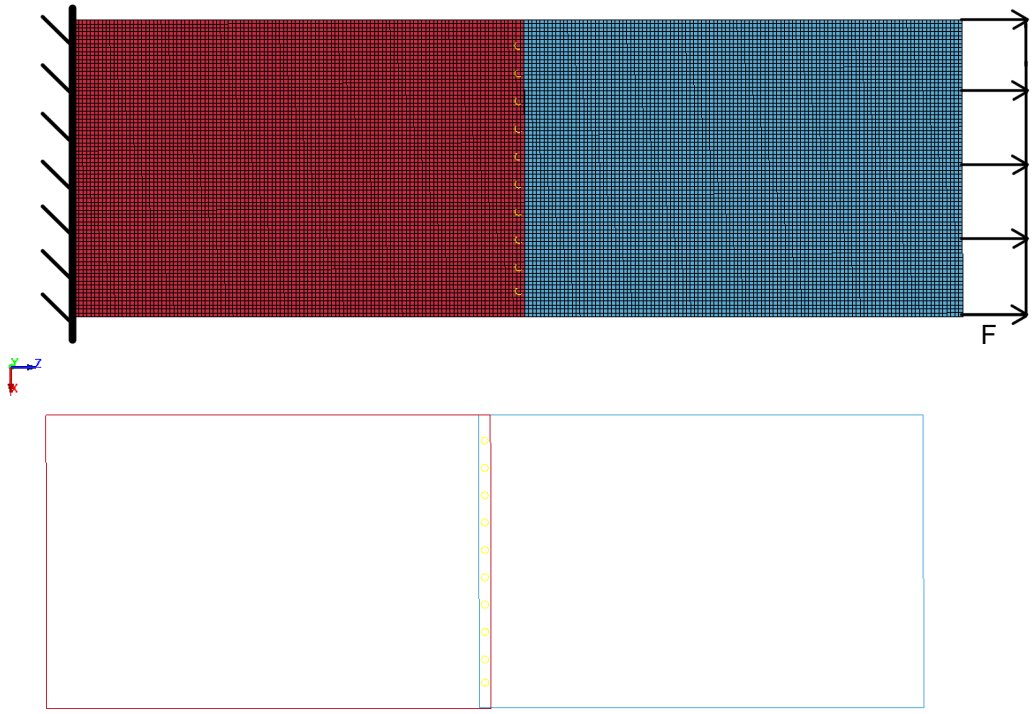

Fig.7: Configuration of the plates and boundary conditions

The red plate, located on the top in the view shown in Figure 7, is fixed at its leftmost end; thus, all three translations and rotations are constrained. A distributed load F is applied to the blue plate in the positive z-direction, ramping up to its maximum value over 20 ms and then remaining constant for the total duration of the analysis, which is 30 ms.

3.3.2 Results

The results show that the force is distributed almost uniformly across the ten rivets, except the two outer rivets, on which stress concentrations are known to develop in tensile cases, exceeding those present at the center of the specimens. Additionally, due to the model's requirements, the lower rivet's pitch is smaller than the others; this will be evident from the slight discrepancies in the forces recorded at the outer rivets.

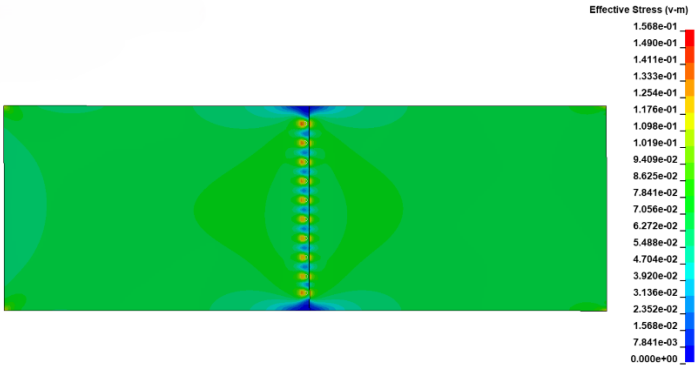

Fig.8: Von Mises stress on the plates

In the two test cases, the distributed force applied at the end was 20 kN in the first case and 16 kN in the second. In the first case, a sequential failure of the rivets was observed; on the other hand, in the second case, the external load was intentionally reduced to achieve only plastic deformation.
Figure 9 presents the results of the axial force components on the left and the shear force components on the right for the simulation where the applied load is 20 kN. The shear force components increase more rapidly in the region where the material exhibits elastic behavior, while from 10 ms forward, the influence of plasticization becomes apparent, initially affecting the outermost rivets. This plasticization distributes the shear load more evenly across the 10 rivets. It is crucial to note that the axial component increases rapidly in the plastic phase and plays a significant role in the overall force computation.

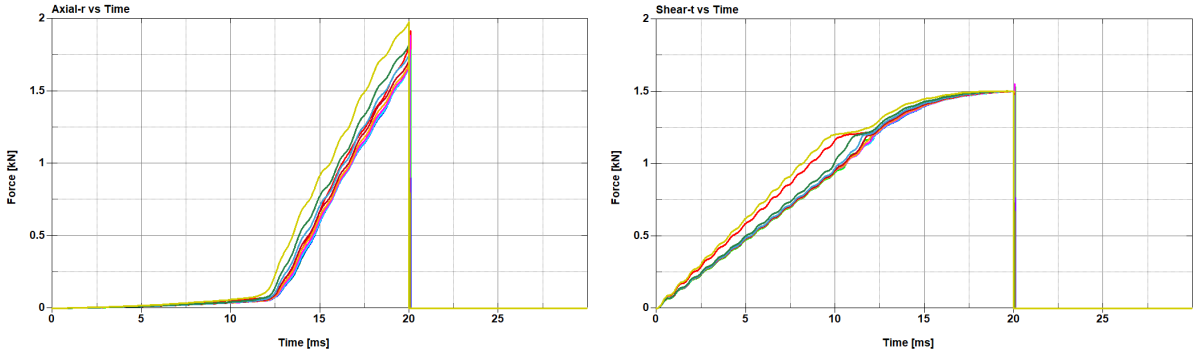

Fig.9: Forces on the rivets with an applied load of 20 kN

At around 20 ms, component failure occurs as equation, previously described in the formulation section, is satisfied. The trend of this function, shown in Figure 10, illustrates how the last rivet, being the most stressed as discussed earlier, is the first to fail. This leads to a sharp increase in the other curves, which physically represents the redistribution of the load across the remaining rivets.

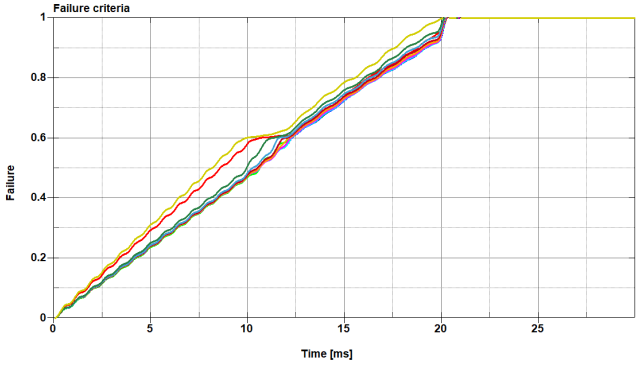

Fig.10: Trend of the function that defines the failure criterion.

Figure 11 shows the trend of both force components on the rivets for the case where the applied load is 16 kN. Here, as well, it can be observed in the image on the right—perhaps more clearly than in the previous case—that after 12 ms, the beams begin to exhibit plastic behaviour. As in the previous case, the most stressed one is the first to enter the plastic region, and once all the rivets have surpassed

their elastic behaviour, their curves for shear forces begin to overlap.

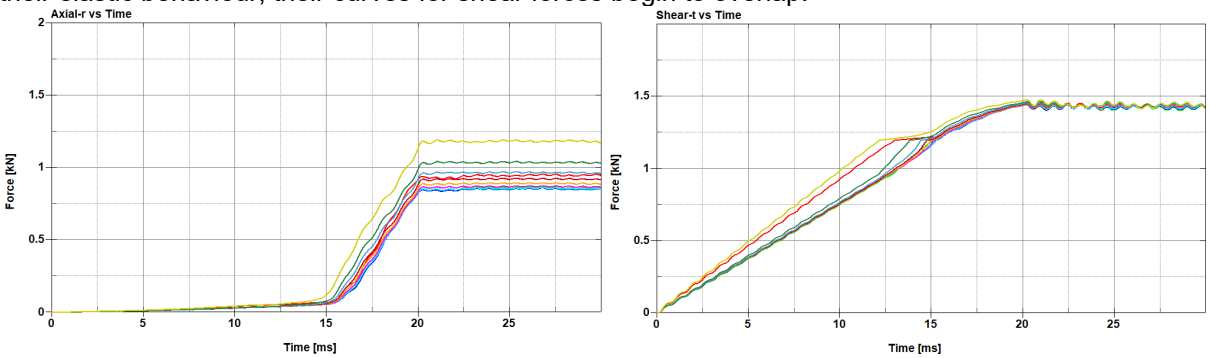

Fig.11: Forces on the rivets with an applied load of 16 kN

In this case, the failure criterion is not met, and therefore no rivet fails.

4 Water impact simulation

4.1 Analytical theories

The topic of water impact has been studied for approximately a century, yet due to its complex nature, there is still no comprehensive formula in the literature that accounts for every scenario. The first to develop a theory was von Karman [1], who considered a simple and symmetric structure.

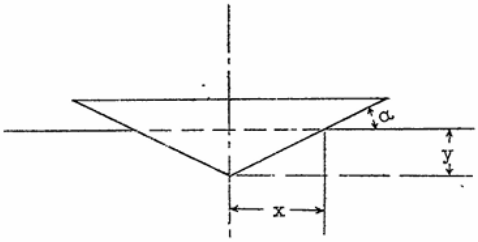

Fig.12: Rigid wedge considered in von Karman and Wagner's theory

Under the assumptions of a rigid body, incompressible fluid, and calm water surface, he derived the following formulation based on the conservation of momentum:

$$P_{VK}(x) = \frac{\rho V_0^2}{2} \frac{\pi}{\left(1 + \frac{\gamma \pi x^2}{2W}\right)^3} cot\ (\alpha)$$

It can be intuitively derived that the maximum occurs when the x-coordinate is zero, corresponding to the keel of the hull, and thus the maximum pressure value is:

$$P_{VK_{max}} = \frac{1}{2}\rho V_0^2 \pi \cot(\alpha)$$

Further efforts were made by Wagner [2], who incorporated a hydrodynamic component into the theory. In this case, the pressure is equal to that found by von Karman only at the keel (x = 0), the point of initial impact where the body's deceleration can be approximated as zero. For brevity, additional details, available in [2, 3], are not provided here. However, the function for maximum pressure is presented, even if it will not be used later in the comparisons.

$$P_{W_{max}} = \frac{\rho V_0^2}{2}\left[1 + \frac{\pi^2}{4}\cot^2(\alpha)\right]$$

In both equations, it can be observed that the maximum pressure depends solely on the water density (ρ), initial velocity (V_0), and dihedral angle (α). In the case where the dihedral angle is zero, both equations, due to the cotangent, tend towards infinity. This is physically impossible and has prompted further research on the problem over the years.

In 1969, Chuang and Sheng-Lun [3] introduced the concepts of trapped air, in cases of low dihedral angles, and elastic wedge, while studying various cases in the naval field. Based on the interpolation of experimental data, the authors correlated the pressure to the square of the initial impact velocity through

a specific coefficient. Considering velocities in fps and pressures in psi, for zero dihedral angles in particular, the relationship is given by:

$$p_{max} = 0.68 * V_0^2$$

In the more recent study [4], the two authors investigate the problem of water impacts on flat surfaces, aiming to address how to estimate pressures in cases of trapped air. Beyond the proposed formulas, which are omitted for brevity, it is noteworthy how the problem has been deconstructed. Specifically, as the dihedral angle varies, three regions are identified:

1. Trapped-air region (a): for angles between 0° and 1°, where the effect of the air cushion is predominant.
2. Transitional region (b): for angles between 1° and 3°, where both the trapped air effect and Wagner-type behavior are observed.
3. Wagner-type region (c): for dihedral angles greater than 3°, where the trapped air effect is not significant, and the pressure behavior follows Wagner's model.

This can be summarized in the following images (Figure 13).

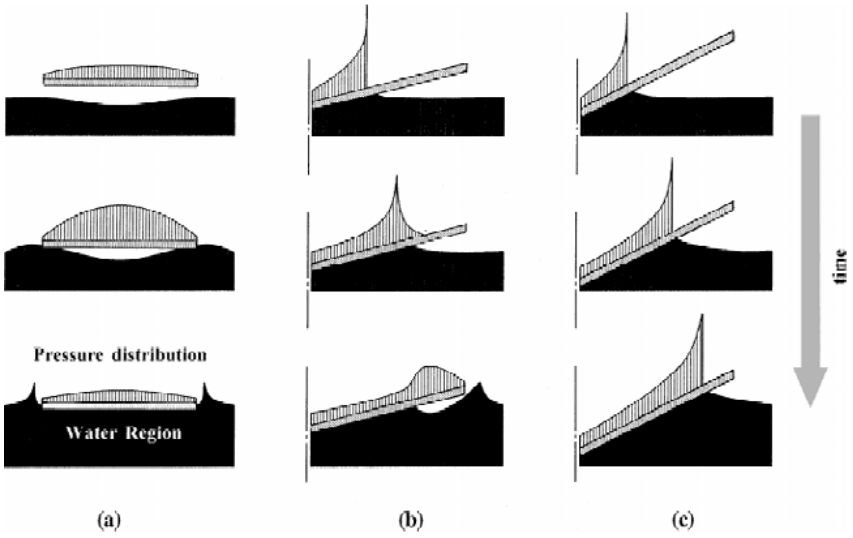

Fig.13: Wedge behaviour upon impact according to Okada-Sumi [4].

They also highlight that, although the pressure peak is lower in the case of trapped air compared to the case with a dihedral angle of 3°, the recorded deformations are greater.

4.2 Numerical model

In this study, the analysis of rivets was applied to a component with dimensions compatible with an aeronautical box located in the subfloor of a helicopter, as shown earlier in Figure 1. The main elements, recreated in SolidWorks, are the stringers, ribs, and panels. In this model, there are two ribs and two stringers framing a panel, which will be the part impacting the water. The components are connected at the interface between one element and the flange of the other through rivets.

The box has dimensions of 970 mm x 830 mm, with the longer side being the one that flexes upon water impact. The material assigned to both the plate and the ribs and stringers is the 2024 aluminum alloy, as previously discussed. A longeron and a rib are shown below, in Figure 14, to provide a clearer view of the dimensions and geometry.

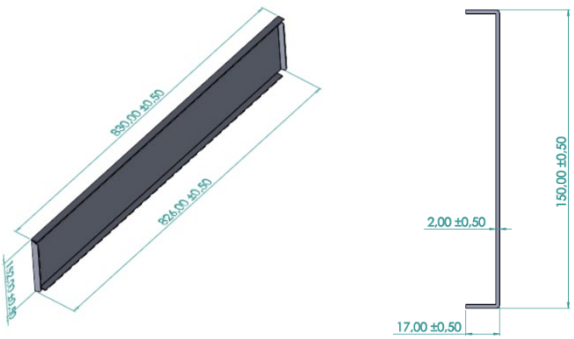

Fig.14: Stringer (left) and section of the rib (right).

The length of the ribs matches that of the body, the height is 150 mm, and the width of the connecting flanges is 15 mm. The components have a thickness of 2 mm, except for the lower plate, which has a thickness of 3 mm. From the geometries, the average surfaces were extracted, discretized using a quadrilateral mesh along with a small percentage of triangular elements, which constitute less than 2% of the total. Denser regions are present near the rivets to ensure accurate results, while sparser regions are in areas of lesser interest to reduce computational cost. Specifically, a square mesh with a side length of 5 mm is implemented near the connections, while a mesh finish of 10 mm is applied in the centre. A total of 136 rivets are arranged with a spacing of 30 mm. To emulate a realistic condition, where a fuselage must support a portion of the helicopter's weight proportional to its dimensions, a mass of 164 kg was added to the upper nodes of the stringers and ribs. The self-weight of the five components of the fuselage is 10.19 kg.

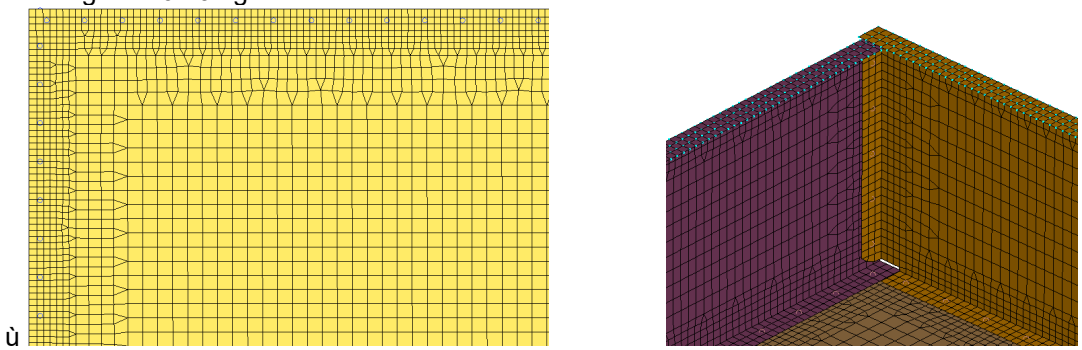

Fig.15: Mesh of the components in a corner of the fuselage.

The water was modelled using the Smoothed Particle Hydrodynamics (SPH) method, which is widely used for simulating fluids that, unlike solids, exhibit large deformations. Its advantage, which distinguishes it from other methods in the literature, is that it is mesh-free; this allows the particles to undergo significant displacements without compromising accuracy. The computational domain measures 2000 x 830 x 200 mm³ and contains 1,660,000 elements. The properties assigned to the SPH were based on the ***MAT_NULL** and the equation of state ***EOS_GRUNEISEN**. The defined parameters refer to water under standard conditions (1 atm, 25 °C).

The boundary conditions employed in the model are as follows: a rigid wall is placed at the bottom, while a wall emulating the infinite downstream (located on the left side in Figure 16) is defined using the keyword ***BOUNDARY_SPH_NON_REFLECTING**. Additionally, symmetry walls are established in the other directions to avoid edge effects, which are defined through the keyword ***BOUNDARY_SPH_SYMMETRY_PLANE**.

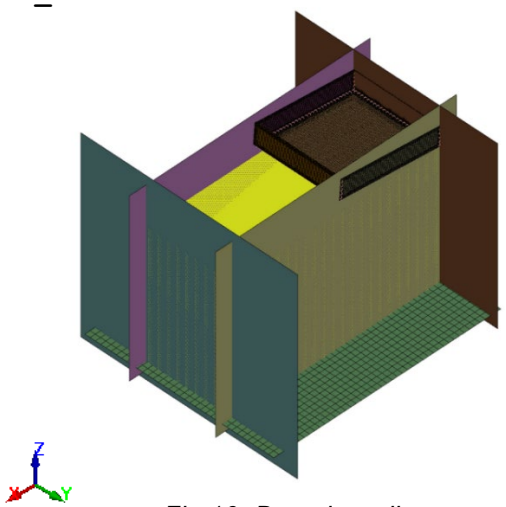

Fig.16: Domain walls

Based on the presented model, nine analyses were conducted, varying the parameters listed in the table.

θ [°]	0 – 2.5 - 5
V_0 [m/s]	1.5 – 2.5 - 5

Table 3: Test cases

In this discussion, five pressure sensors will be considered, as illustrated in Figure 17. These sensors are strategically positioned to measure the pressure exerted on the lower plate of the structure during water impact. The first sensor is located near the keel, adjacent to the symmetry wall; the second one is situated at the centre of the plate and the third one is placed at the free edge of the plate, capturing pressures at the outermost boundary. Finally, the fourth and fifth sensors are positioned at the flexing edges of the plate.

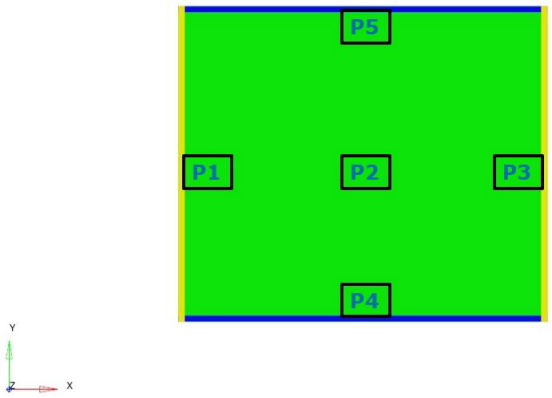

Fig.17: Sensor's position

4.3 Results

These parameters were chosen to understand the geometric and operational range in which a helicopter's subfloor may be situated during a controlled water landing. Specifically, the geometry of the lower plate can be approximated as nearly flat at the centre, or at least characterized by low dihedral angles. Furthermore, during ditching manoeuvres, regulations stipulate that the vertical velocity component should be relatively low, typically below 2.5 m/s, to avoid causing permanent harm to occupants due to sudden decelerations. The analyses conducted yielded results that were consistent with one another and physically realistic. First, the frames depicting the evolution of the fuselage over time are presented in Figure 18, in the case where the vertical velocity is 5 m/s, and the initial dihedral angle is zero.

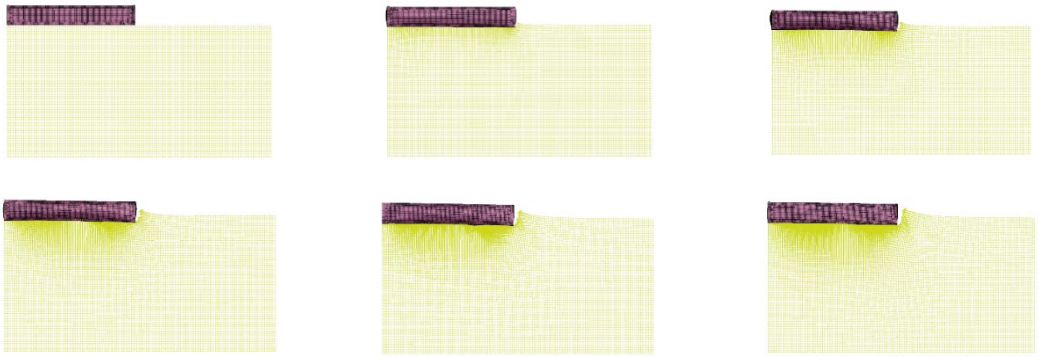

Fig.18: Frames from the analysis of the fuselage with a dihedral angle of 0° and a velocity of 5 m/s

The analyses performed demonstrated rivet failure only when the velocity was equal to 5 m/s, for all the considered dihedral angles. In particular, the results are presented in Table 4.

	1,5 m/s	*2,5 m/s*	*5 m/s*
0°	0	0	31
2,5°	0	0	8
5°	0	0	2

Table 4: Number of failed rivets

It is evident that, for the same dihedral angle, failure occurs at higher impact velocities; similarly, for the same vertical velocity, the scenario where the dihedral angle approaches zero is more critical. This is consistent with findings in the literature [1, 2, 3, 4], which indicate that as the vertical velocity of the body increases, the forces involved also increase.

4.3.1 Analysis with a zero-dihedral angle

Although the effect of air has not yet been considered, the results obtained can be compared with those presented by Okada-Sumi. They report that, as the dihedral angle decreases, there is not only a reduction in pressure due to the damping effect but also an increase in plate deformation. In fact, this effect, along with the deformation of the boundary elements in our case, generates the shear forces on the rivets, leading first to plasticization and subsequently to failure. The following images (Figure 19, 20, 21) present the failure criteria for the rivets in the analyses where failure occurs, similar to what was discussed in the previous chapter, along with the location where it takes place. The axial and shear forces on the rivets are not reported for the sake of brevity.
From the images, it is possible to confirm the data reported in the previous table and, in addition, observe where the failures occur. Focusing on cases where the body impacts the water with a vertical velocity of 5 m/s, it can be noted that failures occur on the right-hand side when the dihedral angle is 0° and 2.5°. In the 0° case, the affected area is more extensive.
The failures likely occur due to the acceleration caused by the impact and buckling in the plate and boundary elements. However, the case with a 5° dihedral angle presents a different scenario, where the two failed rivets are located on the flange connecting the stringer and the ribs. Determining the exact cause is challenging due to the phenomenon's complexity, but it is observed that a second smaller pressure peak occurs in the keel area around the time of failure.

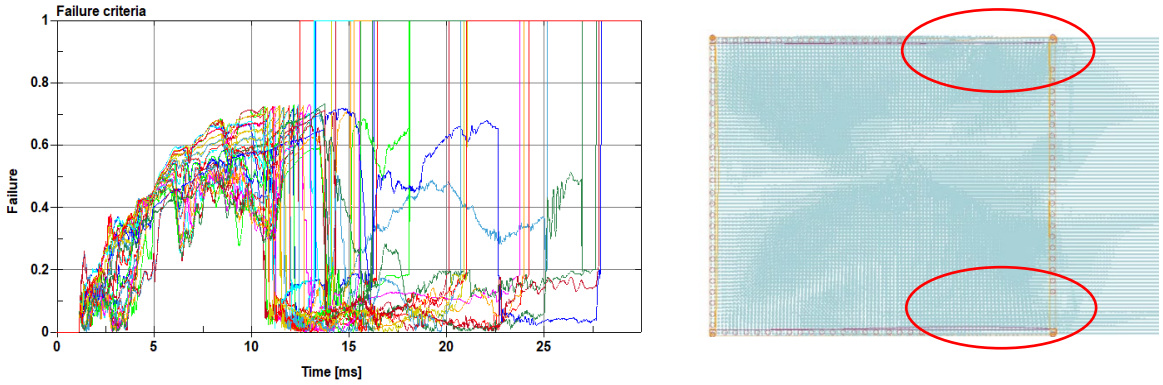

Fig.19: Failure criterion (on the left) and rupture location in the box (on the right) for the analysis with a 0° dihedral angle and a velocity of 5 m/s.

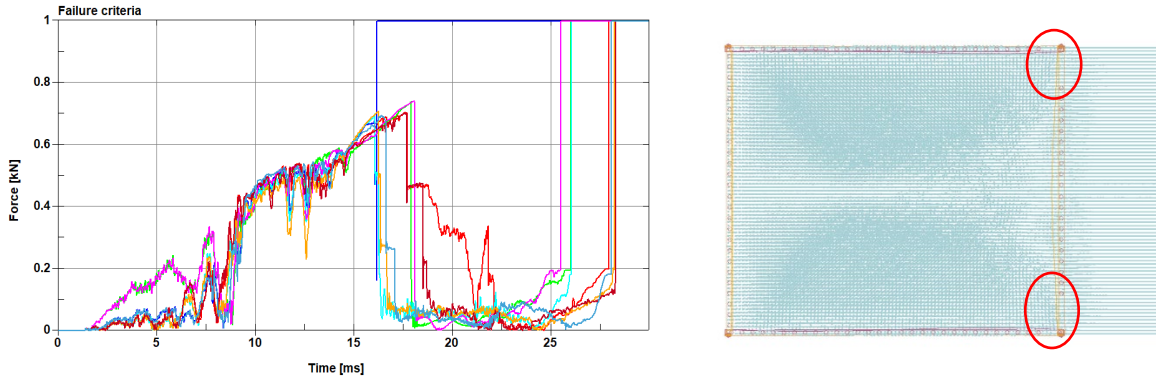

Fig.20: Failure criterion (on the left) and rupture location in the box (on the right) for the analysis with a 2,5° dihedral angle and a velocity of 5 m/s.

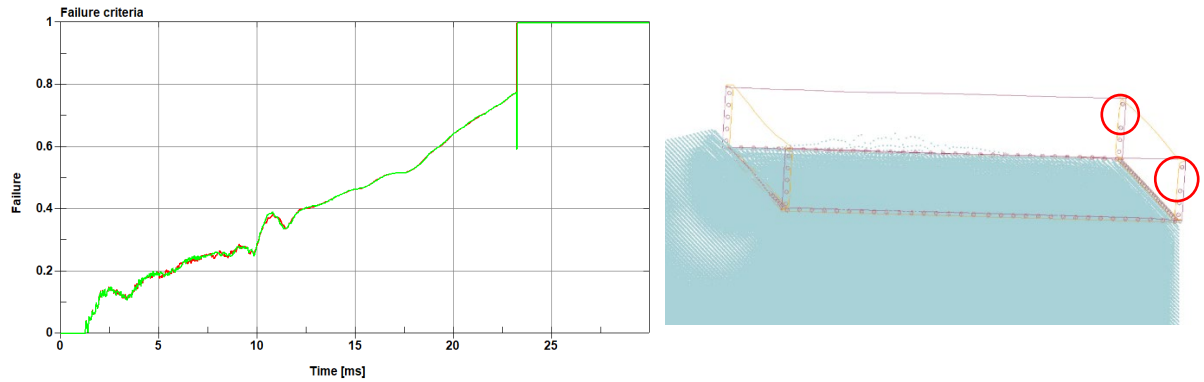

Fig.21: Failure criterion (on the left) and rupture location in the box (on the right) for the analysis with a 5° dihedral angle and a velocity of 5 m/s.

4.3.2 Analysis with a zero-dihedral angle

Another noteworthy result, which echoes the findings of the two Japanese researchers in a previous study [11], concerns the case of a 0° dihedral angle. Specifically, it refers to the distribution of pressure, with the maximum being measured at the center and decreasing toward the edges.
Using three pressure sensors along the length of the lower plate - one positioned near the keel, one at the centre of the plate, and the last at the free edge - it was possible to obtain the maximum pressure values and assess the deviation of the edge values from the maximum, which occurs at the central sensor. Considering B as the body's span, Figure 22 shows the pressure distributions, each normalized to its respective maximum, across the body for the three velocities under study.
Two observations can be made: the first concerns the fact that, as defined in the model, there is a higher pressure at the free end; the second relates to the trend of the curves, specifically that the greater the velocity, the larger the pressure difference between the centre and the edges.

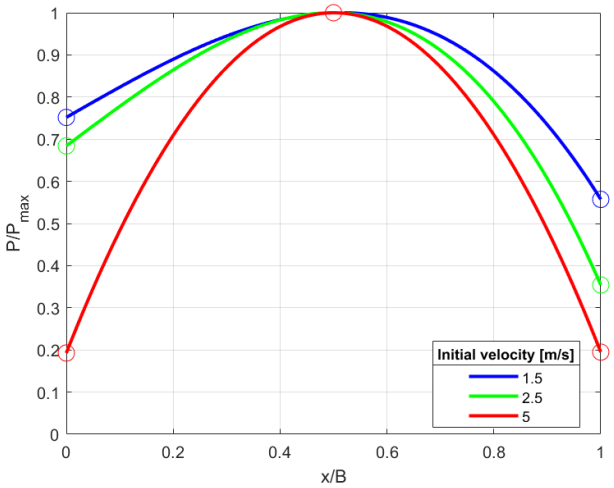

Fig.22: Pressure distribution along the span of the lower plate.

Focusing exclusively on the analyses where the dihedral angle of the cassettes is zero, the maximum pressure results were compared with varying impact velocities. The comparison, shown in Figure 23, was made with the experimental curve obtained by Chuang and Sheng-Lun [3] for a 0-degree angle, as well as with the Okada-Sumi theory [4], considering both the symmetric and asymmetric cases.
The results indicate that the collected data align more closely with the first theory. This is likely due to the boundary conditions applied in our case, which, as in the theory [3], assume that the lower plate is constrained by the frame elements and thus less free to flex. Moreover, the mass of our body is comparable to the case presented in [3] and significantly larger than that presented in [4], which may explain why the higher inertia led to higher recorded pressures. Additionally, a discrepancy is observed between our model and the theory [3] as the velocity increases; this behaviour arises because the elasto-plasticity of our model reduces the recorded pressure, whereas Chuang and Sheng-Lun assume a rigid plate.

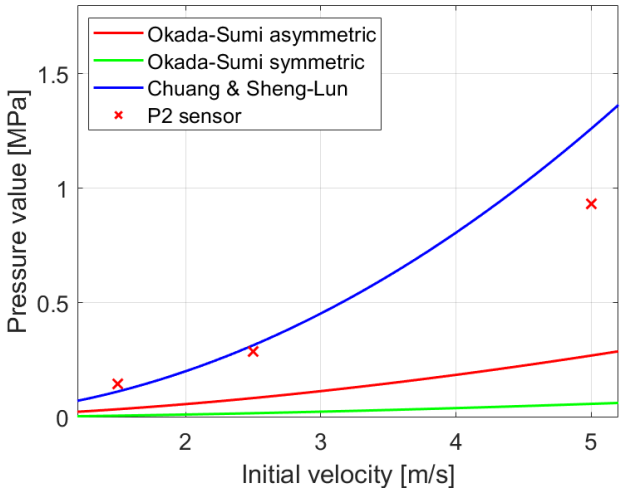

Fig.23: Maximum pressure in cases where the dihedral angle is zero

4.3.3 Air introduction for 0° case

The cases analysed so far do not account for the formation of air cushions, as air is not present in the model. This was later introduced through a volume of particles, modelled using the SPH method, placed above the water volume in which the body is submerged. The properties were assigned using the ***MAT_NULL** and ***EOS_LINEAR_POLYNOMIAL** keywords, and a wall was added above the entire volume to simulate the column of air present above the control volume. The contacts between the air volume, the body, and the water are defined, with the interaction between the air and water specifically managed using the keyword ***DEFINE_SPH_TO_SPH_COUPLING**.
The most critical case, characterized by the maximum speed and the minimum dihedral angle, was analysed with the presence of air to assess how the air cushion would affect the rivet failure. This analysis aimed to determine the impact of the air cushion on altering the failure value. The analysis results confirmed the formation of an air cushion, which deforms the lower plate and mixes with the underlying water (Figure 24) but highlighted that no rivet breaks.

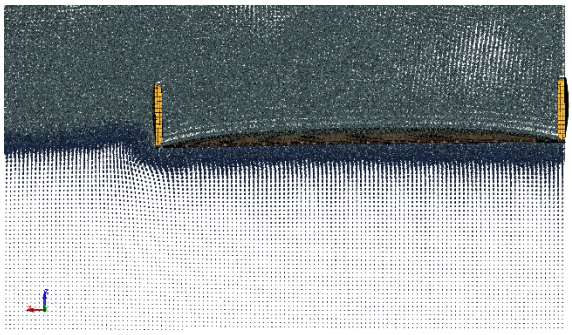

Fig.24: Box impacting water with the presence of air in the model

Additionally, the pressure distribution on the plate is more uniform, with the maximum discrepancy around 10%, in contrast to the cases without air where the difference reaches up to 80%. The results obtained from five sensors, described before, positioned at the centre of the plate and at the midpoints of each of the four sides near the edge are presented in Figure 25. It is evident that the obtained values closely resemble the findings from study [4] when the body is considered symmetrical, meaning that the width of the model is only half of the actual size. This symmetry is defined in our model through the previously discussed wall.
Although close to the theory, the results were not considered entirely realistic due to a significant amount of air remaining trapped. This issue is likely aggravated by the fact that the problem is modelled in two dimensions, and there is a non-negligible decrease in velocity prior to the impact with the water, even if slight. Further analyses will be conducted in the future to investigate this issue.

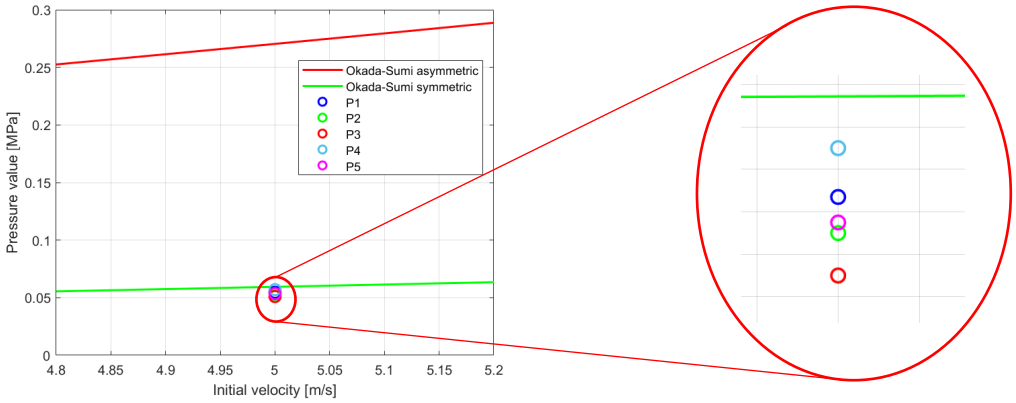

Fig.25: Results of the impact analysis at 5 m/s with a zero-degree dihedral angle and air included in the model.

4.3.4 Analysis with a dihedral angle of 5°

The case of a 5° dihedral angle falls within those where air is not trapped beneath the body, and thus no significant reduction in the measured pressures is observed. This is also the angle at which von Karman's theory begins to hold, as it avoids the excessively high values seen at lower dihedral angles due to the cotangent in the formula's numerator. The results obtained through numerical analysis are compared with the maximum pressure predicted by von Karman [1] and the experimental formulation presented by Chuang and Sheng-Lun [3] in Figure 26.

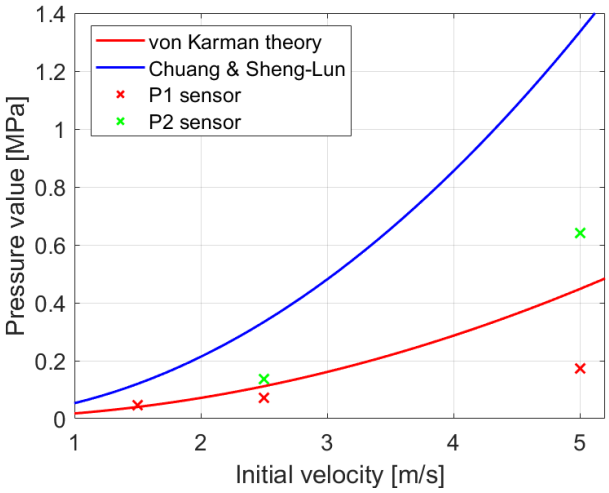

Fig.26: Comparison of maximum pressures for a 5° dihedral angle

For the second case, the formulation for a 6° dihedral angle was used, as there is no available formula for 5°. The recorded values are shown for both sensor P1, located near the keel, and sensor P2, positioned at the centre of the structure.
The discrepancy in the results can be attributed to several factors. The most significant one is the elasto-plasticity of the structure. As previously discussed, the deformability of the body reduces the peak pressure. This factor is particularly evident when compared with the theory of Chuang et al. [3], where despite the lower angle considered in the numerical analysis, it does not result in higher pressure. Additional causes of discrepancies in the pressure readings may stem from the fact that during the ditching process, the body rotates, reducing its dihedral angle, and the lower plate undergoes buckling, locally altering the dihedral angle in both directions. As in the previous discussion, the effects of the body's elasticity become more pronounced as the velocity increases. This results in lower velocity cases producing values that align more closely with analytical theories.

4.3.5 Comparison of results at sensor P1

Finally, a comparison is made between the pressure results recorded by sensor P1 across the nine case studies (Figure 27). The pressure is plotted as a function of the dihedral angle and initial impact velocity for the sensor closest to the keel, as this avoids comparing cases where the presence of air could have a significant influence. In particular, it is clearly observed that the pressure increases up to 2.5° and then decreases as the dihedral angle increases, as predicted by earlier theories. The peak in the intermediate

case is also reported by Okada-Sumi [4] regarding the results obtained by Chuang and Sheng-Lun [3], which becomes evident when considering the velocity scaling factors.

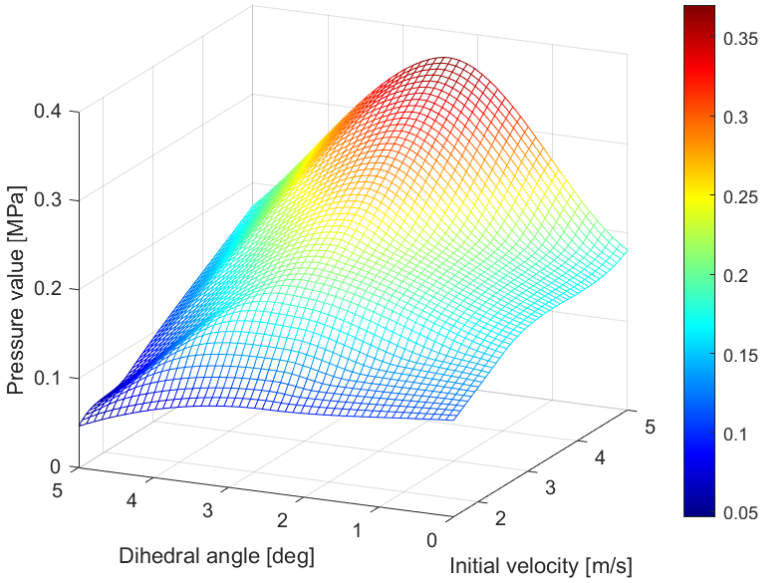

Fig.27: Pressure as a function of the dihedral angle and impact velocity

In general, it is evident that as the impact velocity increases, the pressure peak rises for every dihedral angle considered. The overall trend is consistent with findings in the literature, although the comparison models do not account for the presence of air. Two key factors likely influence the results: the flexibility of the body, which increases as the dihedral angle decreases, and the impact surface area. In the case of a 0° dihedral angle, early theories [1, 2] considered only the geometric factor of the angle itself, failing to account for the possibility of reduced pressure at low or zero dihedral angles. This has since been disproven [3, 4], as a larger contact surface allows for more effective distribution of pressure. Additionally, the phenomenon is significantly more complex, requiring consideration of factors such as potential deformations, air cushions, and the inertia of the impacting body.

5 Summary

This study aimed to develop an effective modeling approach for aerospace rivets and apply it to a ditching scenario. After conducting thorough analyses, the rivets were modeled using beam elements, to which appropriate characteristics were assigned, and subsequently, they were connected to the components via contact definitions. Alternative modeling approaches can still be effective in cases where solid elements are employed, when the mesh is sufficiently refined that failure would occur first in the sheet metal, or when the applied forces are low enough to ensure that failure does not occur. The beam and contact modeling method also offers the advantage of allowing for the definition of specific materials and the placement of elements independently of the mesh.

In the second part of the study, the impacts of a helicopter fuselage on water were examined. Analytical theories and experimental results formulated by various researchers over the years were presented and compared. Initially, the focus was on the rivets that failed due to the impact. This was followed by an investigation of the pressures developed on the lower plate. In analyses where air was not modeled, the recorded results near the keel mirrored those found in the experiments conducted by Chuang and Sheng-Lun. For zero dihedral angles, the pressures followed the trends predicted by Okada-Sumi, although the maximum values differed, likely due to factors such as boundary conditions, material elasticity, and inertia. When air was incorporated into the model, the resulting values closely aligned with the aforementioned theory. For a dihedral angle of 5°, the von Karman theory was considered, and the results obtained showed values that approached this theoretical framework.

In conclusion, the topic of water impacts is extremely complex, and no single theory encompasses all possible scenarios. This study aims to serve as a starting point for future developments on more complex models in the aerospace sector.

6 Literature

[1] von Kármán T. “The impact on seaplane floats during landing” NACA Technical Notes N.321, 1929.

[2] Wagner, H. “Phenomena Associated with Impacts and Sliding on Liquid Surfaces”, NASA Techdocs, 1932.

[3] Chuang, Sheng-Lun. “Investigation of impact of rigid and elastic bodies with water”, The Catholic University of America, 1969.

[4] Okada, S., Sumi, Y. “On the water impact and elastic response of a flat plate at small impact angles”. Journal of Marine Science and Technology, 2000, 5. 31-39. 10.1007/s007730070019.

[5] Korobkin, A. “Cavitation in liquid impact problems”. In Proceedings of the Fifth International Symposium on Cavitation (CAV2003), Osaka, Japan, 1 January 2003; Volume 2, pp. 1–7.

[6] Kevin Hughes, Rade Vignjevic, James Campbell, Tom De Vuyst, Nenad Djordjevic, Lampros Papagiannis. “From aerospace to offshore: Bridging the numerical simulation gaps–Simulation advancements for fluid structure interaction problems”, International Journal of Impact Engineering, Volume 61, 2013, Pages 48-63, ISSN 0734-743X.

[7] CAST. “Crashworthiness of helicopters onto water e design of structures using advanced simulation tools”, funded by the European Community under the ‘competitive and sustainable growth’ programme (Contract G4RD-CT1999 0172), 2000e2003

[8] B. Langrand, E. Deletombe, E. Markiewicz, P. Drazétic, “Riveted joint modeling for numerical analysis of airframe crashworthiness”, Finite Elements in Analysis and Design, Volume 38, Issue 1, 2001, Pages 21-44, ISSN 0168-874X.

[9] Livermore Software Technology. (2023). LS-DYNA Multiphysics Manual. Retrieved from https://ftp.lstc.com/anonymous/outgoing/web/ls dyna_manuals/DRAFT/DRAFT_Vol_I.pdf.

[10] Passuti, M., Villa F. (2011/2012). "Soluzione innovativa di sottopavimento di elicottero per impatto su acqua"

[11] Okada S, Sumi Y (1995) Experimental study on the maximum pressure and the duration time of the horizontal water impact of flat plate (in Japanese). J Soc Nav Archit Jpn 178:381 389